CrossMark

J. Fluid Mech. (2021), *vol*. 908, R1, doi:10.1017/jfm.2020.877

JFM RAPIDS
journals.cambridge.org/rapids



Hypersonic shock impingement on a heated flat plate at Mach 7 flight enthalpy

Eric Won Keun Chang[1], **Wilson Y. K. Chan**[1], **Timothy J. McIntyre**[2] and **Ananthanarayanan Veeraragavan**[1],†

[1]Centre for Hypersonics, School of Mechanical and Mining Engineering, The University of Queensland, Brisbane, Queensland 4072, Australia

[2]Centre for Hypersonics, School of Mathematics and Physics, The University of Queensland, Brisbane, Queensland 4072, Australia

(Received 26 August 2020; revised 23 September 2020; accepted 12 October 2020)

Elevated wall temperatures and impinging shock interactions are prevalent features in hypersonic flight. Currently, there is a lack of literature regarding experimental studies examining both features in a flight-representative environment. This work details hot-wall, hypersonic, impinging shock/boundary-layer interaction experiments performed in the T4 Stalker Tube. The model configuration was a two-dimensional heated flat plate and a shock generator. The surface of the graphite flat plate was resistively heated to a mean temperature from $T_w = 298$ K to $T_w \approx 675$ K during an experimental run. An oblique shock, generated by a plate that was inclined at 10° or 12° to the free stream, was impinged on the heated flat plate to induce boundary layer separation. The primary flow condition produced Mach 7 flight-equivalent nozzle-supply enthalpy with a unit Reynolds number of 4.93×10^6 m^{-1}. More flow conditions with lower unit Reynolds numbers and flow enthalpies were considered to examine flow separation characteristics. Schlieren and infrared thermography captured the flow field and the wall temperature distribution, respectively. The results showed that the size of the flow separation grew with a higher T_w and a lower unit Reynolds number. Moreover, the scaled separation of the present data showed a high discrepancy with existing separation correlations developed from a supersonic impinging shock and a hypersonic compression ramp, mainly due to the higher shock strength. Instead, the present data followed a scaling law that includes the pressure ratio across the impinging shock with a slight dependence on the wall temperature ratio.

Key words: high-speed flow, boundary layer separation, shock waves

† Email address for correspondence: anandv@uq.edu.au

© The Author(s), 2020. Published by Cambridge University Press

https://doi.org/10.1017/jfm.2020.877 Published online by Cambridge University Press

1. Introduction

Impinging shock/boundary-layer interaction (SBLI) causes an adverse pressure gradient that leads to boundary layer separation with higher surface pressure and heat load, occurring across the internal and external surfaces of hypersonic vehicles (Dolling 2001). In the case of scramjet flowpaths, engine unstart might occur due to a large-scale boundary layer separation (Gai & Khraibut 2019). On the vehicle airframe, extreme local pressure and heat loads require structural/thermal protection considerations. Given the complexity of the fluid phenomenon and the relative infancy of our understanding, numerous experimental investigations have been conducted using 'canonical' models to better understand these complex flow features.

Previous SBLI experiments in hypersonic impulse facilities examined the high-temperature aerothermodynamic effects of flow separation in various model configurations. Such configurations include compression ramp/double wedge (Mallinson, Gai & Mudford 1997; Bleilebens & Olivier 2006; Swantek & Austin 2015; Knisely & Austin 2016; Wagner *et al.* 2018) and impinging shock (Sandham *et al.* 2014; Sriram & Jagadeesh 2015; Sriram *et al.* 2016). In the two-dimensional impinging shock configuration, Sandham *et al.* (2014) observed enhanced transition from impinging an oblique shock with a deflection angle of 2° and 4° at Mach 6; however, the shock strength was not sufficient to fully separate the boundary layer. Researchers at the Indian Institute of Science (Sriram & Jagadeesh 2015; Sriram *et al.* 2016) utilised a model with higher deflection angles of 27° or 31° to examine the laminar separation length L_{sep}, the streamwise distance from the start of the separation to the impingement point. An inviscid scaling law between L_{sep} and the reattachment pressure ratio was developed using their data.

In addition, the wall temperature T_w has been observed to act as an important parameter in flow separation. During their high-dynamic-pressure trajectory (Billig 1993), scramjets experience radiative wall cooling and internal heat transfer so T_w equilibrates lower than the recovery temperature T_r; also, the wall-to-total temperature ratio T_w/T_s will be much smaller than 1. Nonetheless, T_w will be several times higher than the free-stream temperature T_∞; therefore it changes the boundary layer properties and the extent of flow separation. Since the change in T_w is negligible during the millisecond-order test duration of impulse facilities, model preheating has been employed to simulate realistic thermal conditions of hypersonic flight. Early efforts by Elfstrom (1972) used preheating of a compression-ramp model in a gun tunnel that achieved $T_w/T_s = 0.68$ at Mach 9.22 to examine the effect of elevated T_w on flow separation. Bleilebens & Olivier (2006) also preheated the surface of a compression-ramp model at a higher nozzle-supply enthalpy $H_s = 5.0$ MJ kg^{-1} flow in a shock tunnel, and developed a modification of the scaling law of Katzer (1989) to better account for T_w. Recent works by Wagner *et al.* (2018) have also explored the effect of a heated wall in a large-scale compression-corner model. Experimental data on an impinging SBLI configuration with hot walls in high-speed flows are scarcer than compression-corner studies. Jaunet, Debieve & Dupont (2014) observed a growth of L_{sep} with the heated wall that achieved wall-to-recovery temperature ratio $T_w/T_r = 1.9$ at Mach 2.3 supersonic flow. No hypersonic experimental data are currently available exploring the heated-wall, impinging SBLI configuration. The most relevant work is the numerical work of Volpiani, Bernardini & Larsson (2020) that simulated a heated (isothermal) wall boundary condition for the unheated Mach 5 impinging SBLI experiments (Schülein 2006).

https://doi.org/10.1017/jfm.2020.877 Published online by Cambridge University Press

Condition	M_∞ ±2.0 %	Re_∞ ($\times 10^6$ m^{-1}) ±7.6 %	p_s (MPa) ±3.6 %	H_s (MJ kg^{-1}) ±3.3 %	T_s (K) ±2.5 %	p_∞ (Pa) ±13 %	T_∞ (K) ±5.1 %	u_∞ (m s^{-1}) ±1.5 %
A	7.00	4.93	15.5	2.43	2334	2569	251	2225
B	7.07	1.57	4.1	2.17	2147	671	223	2121
C	7.29	3.23	5.4	1.53	1652	846	156	1829
D	7.36	3.70	5.2	1.31	1475	782	135	1717

TABLE 1. Mean facility nozzle-supply (subscript s) and free-stream (subscript ∞) properties of the present experiments.

The work reported herein presents experimental results concerning shock impingement on a heated flat plate at high-Mach-number flight test conditions, which has not been explored previously in the literature. In recent work (Chang *et al.* 2020), the authors found that the flat plate boundary layer thickened with higher T_w from the hypersonic flow testing of a heated flat plate. In the present study, the authors installed a shock generator to generate a strong oblique shock to separate the flat plate boundary layer. With the preliminary numerical simulations (Chang *et al.* 2019) predicting the growth of flow separation with wall heating, the authors aim to experimentally characterise and quantify the behaviour of flow separation for an impinging-shock heated-flat-plate model subjected to hypersonic flow in the University of Queensland's T4 shock tunnel.

2. Experimental details

2.1. *Test facility and flow conditions*

All experiments were conducted in the T4 Stalker Tube (reflected shock tunnel) at the University of Queensland, Australia. T4 utilises piston compression of the driver gas to generate high nozzle-supply pressures and temperatures for a wide range of hypersonic flight conditions (Stalker *et al.* 2005). Table 1 shows the mean nozzle-supply and free-stream (nozzle-exit) properties of a Mach 7 axisymmetric nozzle (Chan *et al.* 2018). Conditions A and B examined Mach 7 flight enthalpy at pressures equivalent to flight at 25 and 33.5 km, respectively. Conditions C and D produced 'off-design' flow conditions with Mach 5.5 (1.53 MJ kg^{-1}) and 5.0 (1.31 MJ kg^{-1}) flight enthalpies. ESTCj (Jacobs *et al.* 2014) was used to calculate the properties, and the experimental uncertainties were computed by the process outlined in Mee (1993). The real-gas effects in the nozzle expansion were negligible at these low-enthalpy conditions, because the mass spectrometer studies of the nozzle supply and free stream in the T4 Stalker Tube (Boyce, Takahashi & Stalker 2005*a*,*b*) showed good agreement with ESTCj calculations assuming chemical equilibrium up to ≈3 MJ kg^{-1}.

2.2. *Experimental model and flow diagnostics*

Figure 1 shows a schematic of the heated plate model. The flat plate consisted of a 70 mm front section and a 250 mm heated section. The front section had a sharp ($r < 0.1$ mm), replaceable leading edge. Direct-circuit current applied through copper electrodes resistively heated an isotropic graphite plate 250 mm long and 200 mm wide to temperatures T_w that were over 800 K in a minute. The graphite plate was electrically isolated from the model structure using alumina (Al_2O_3) ceramic insulators. Further information regarding the design and testing of the heated flat plate is provided in

https://doi.org/10.1017/jfm.2020.877 Published online by Cambridge University Press

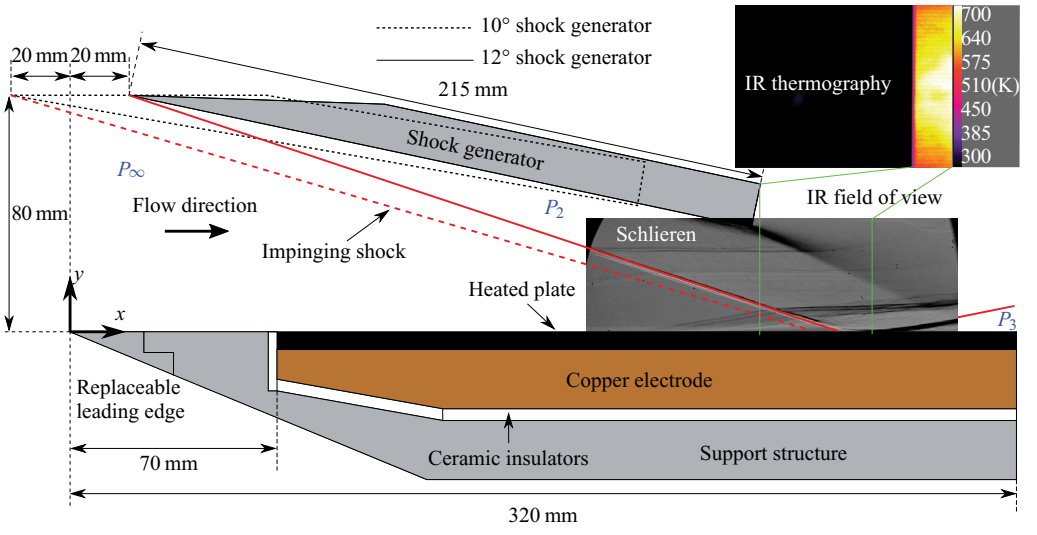


FIGURE 1. Schematic of the heated model and fields of view for optical diagnostics.

Chang *et al.* (2020). In addition to the heated plate, an unheated instrumented plate was also utilised to obtain the quantitative surface data. The instrumented plate had the same surface finish as the heated plate, but a longer length to record the properties downstream of the interaction. The 43 Kulite$^{(R)}$ XTEL-190 (M) pressure transducers were distributed from $x = 121$ mm to $x = 394$ mm in two rows spaced 13 mm apart (centreline and 13 mm spanwise offset). Next to the centreline, 35 thin-film heat transfer gauges were distributed from $x = 102$ mm to $x = 561$ mm with a 13.5 mm spacing. All channels for the sensors were sampled at 1 MHz. Although not shown for brevity, the steady measurement was confirmed in all surface instrumentation within the total available test duration of the T4 Stalker Tube.

A shock generator plate 215 mm long and 172 mm wide was mounted above the heated flat plate. Two deflection angles of 10° (dashed line) and 12° (solid line) relative to the free stream generated inviscid shock strengths of $p_2/p_\infty = 4.38$ and $p_2/p_\infty = 5.53$, respectively. For both deflection angles, the leading edge of the shock generator was positioned 80 mm above the flat plate to avoid interaction with the weak viscous-interaction shock from boundary-layer growth, starting from the flat plate leading edge. In the streamwise direction, the leading edge was positioned 20 mm upstream from the flat plate leading edge for the 10° generator and 20 mm downstream for the 12° generator. This ensured the oblique shock was well displaced from the expansion waves emanating from the trailing edge of the shock generator at the impingement point. From theoretical estimation, the oblique shocks from the 10° and 12° deflection of the $M_\infty = 7$ free stream were expected to impinge at 252 and 260 mm downstream, respectively, from the flat plate leading edge.

The boundary layer height (δ) at the shock impingement location ($x \approx 260$ mm) for Condition A was found to be ≈2.1 mm and ≈2.9 mm for the unheated ($T_w = 298$ K) and heated ($T_w \approx 720$ K) wall cases, respectively, based on our previous results (Chang *et al.* 2020). When heated, the boundary layer thickened and formed 'rope-like' structures at a more upstream location. This suggests that the heated boundary layer may have exhibited transitional behaviour. Figure 2(*a*) shows the measured Stanton number distribution of the undisturbed boundary layer. Here, heat transfer data are presented via the free-stream

https://doi.org/10.1017/jfm.2020.877 Published online by Cambridge University Press

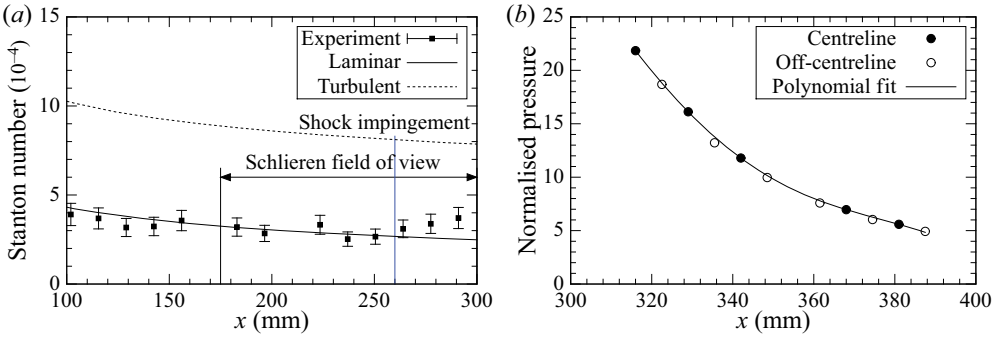


FIGURE 2. Instrumented plate results, Condition A. (*a*) Stanton number of the undisturbed boundary layer. (*b*) Static pressure in two spanwise locations.

Stanton number. Comparison with the theoretical calculation of Cebeci & Bradshaw (2012) confirms that the unheated boundary layer of Condition A is laminar at the shock impingement. Therefore, all other results in the low-Reynolds-number conditions may be considered laminar as well. Next, in order to minimise three-dimensional effects the model was designed to be as large as possible within the Mach 7 nozzle core-flow to keep the flow spillage as far away from the measurement locations as possible. The two-dimensionality is verified by a good agreement between the normalised pressures (by the first sensor at $x = 121$ mm) at the two spanwise locations downstream of the interaction, as shown in figure 2(*b*).

For optical diagnostics, schlieren and an infrared (IR) thermography system were employed to characterise the flow field and plate temperature, as described in Chang *et al.* (2020). The schlieren field of view is shown in figure 1. In the streamwise direction, the field of view covered from $x = 175$ mm to $x = 300$ mm. In the vertical direction, the field of view included the trailing edge of the shock generator, which is 40 mm above the plate surface. The images were captured at 15 000 frames per second with an exposure time of 1 μs. The surface temperature distribution of the plate was captured by a FLIR AC655 camera mounted vertically above the T4 test section. The IR image shown in figure 1 included a portion of a heated plate with a field of view of 30 mm × 95 mm. The calibration technique from the previous work utilising thermocouples was used to estimate the wall temperature of the heated plate in an actual shot (experimental run).

3. Results and discussion

3.1. *Flow establishment*

The millisecond-order test duration (t) in the T4 shock tunnel requires verification to ensure that the flow separation is not evolving temporally during the steady test-time. The time required to establish a steady flow separation, t_{sep}, is examined as follows. For the separation of compression-corner flows in a shock tunnel, Holden (1971) employed the acoustic disturbance to traverse the interaction length, L_{sep}, at the mean speed of sound in the boundary layer, a_δ, to develop $t_{sep} = L_{sep}/a_\delta$. With regard to the present model with $L_{sep} = 90$ mm (maximum field of view upstream of the shock impingement), using this correlation gives an estimate of $t_{sep} \approx 0.18$ ms. Sriram *et al.* (2016) discovered that the t_{sep} values of an impinging shock geometry at $M_\infty = 5.88$ and $M_\infty = 8.54$ were measured to be shorter than the estimates from the correlation of Holden (1971). Further experimental studies using surface heat transfer measurement and flow visualisation

https://doi.org/10.1017/jfm.2020.877 Published online by Cambridge University Press

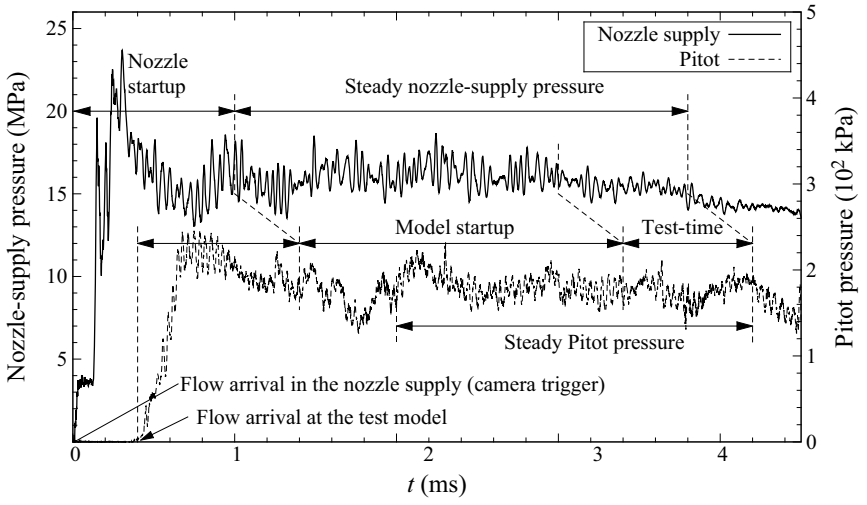


FIGURE 3. Test flow examination from measured piezoelectric pressure signals.

(Swantek & Austin 2015; Knisely & Austin 2016) observed t_{sep} about two to eight flow lengths for compression-corner geometries. For the streamwise length of 320 mm in the present model, two to eight flow lengths results in t_{sep} estimates from approximately 0.29 to 1.15 ms. This is a conservate estimate as L_{sep} will be much smaller than 320 mm.

Measured piezoelectric pressure signals from a representative shot are plotted in figure 3. The t label in the axis represents the time since the data acquisition system was triggered by the reading of the pressure sensor located in the nozzle supply. The nozzle-supply pressure remains fairly steady until $t \approx 3.8$ ms, at which time it starts to drop. The drop in pressure indicates the end of the available steady test-time. Note that driver gas contamination is expected to occur well after the end of the test duration, as approximated using the correlation by Boyce *et al.* (2005*a*). The facility nozzle requires $t \approx 1$ ms (Chan *et al.* 2018) to establish, and the flow requires about 0.4 ms to travel from the nozzle supply to the Pitot probe aligned with the model leading edge. Due to the delay in this flow traversal time, the steady Pitot pressure is only reached at $t \approx 2$ ms and remains steady for ≈2.2 ms. Therefore, in the present study we have sufficient test-time that is greater than the minimum t_{sep}.

In order to accurately characterise the steady separation, the onset of separation was approximated as the location where the separation shock intersects the flat plate, similarly to the method of Sriram *et al.* (2016). For the present study, a linear line fit along the separation shock was extrapolated to the flat plate surface, as illustrated in figure 4(*a*). The shock location throughout the steady inflow on the model is plotted in figure 4(*b*). When $t = 3$ ms, the separation shock gradually moves upstream from 200 mm to 180 mm until reaching a steady location at around $t = 3.5$ ms for the unheated case (filled square symbols in figure 4*b*). The shock position remains relatively steady for about 0.6 ms, labeled as 'test-time' in figure 3. Similarly to the observations of Sriram *et al.* (2016), the separation shock oscillates slightly during the steady inflow, with an amplitude of ±2 mm for the present data. The shock position itself oscillates due to the inherent unsteadiness involved in SBLI and free-stream disturbances in shock tunnel flows. For the heated case (filled circle symbols in figure 4*b*), the steady test-time occurs at $t \approx 3.8$ ms, due to the larger size of the separation bubble. After the steady test-time, the decrease in nozzle-supply pressure causes the separation shock to become unstable.

https://doi.org/10.1017/jfm.2020.877 Published online by Cambridge University Press

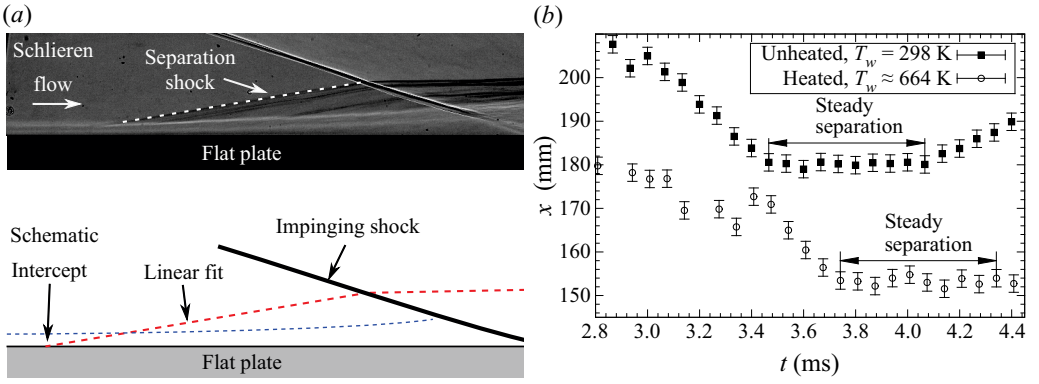


FIGURE 4. Linear fit to determine the separation shock location during the test-time. (*a*) Linear fit. (*b*) Separation shock location.

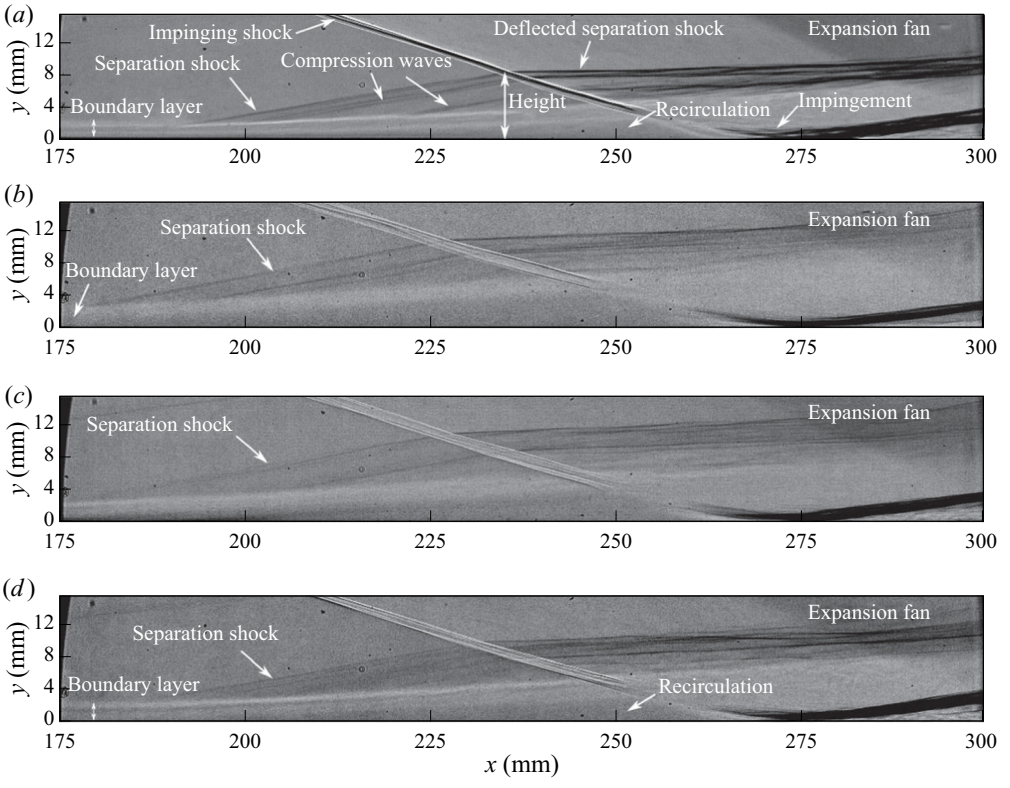


FIGURE 5. Unheated model with impinging SBLI flow field: 12° shock generator. (*a*) Condition A, $T_w/T_\infty = 1.24$, $T_w/T_r = 0.156$, $Re_\infty = 5.25 \times 10^6$ m^{-1}, $t = 3.86$ ms. (*b*) Condition B, $T_w/T_\infty = 1.35$, $T_w/T_r = 0.163$, $Re_\infty = 1.54 \times 10^6$ m^{-1}, $t = 3.85$ ms. (*c*) Condition C, $T_w/T_\infty = 1.92$, $T_w/T_r = 0.222$, $Re_\infty = 3.15 \times 10^6$ m^{-1}, $t = 3.87$ ms. (*d*) Condition D, $T_w/T_\infty = 2.22$, $T_w/T_r = 0.250$, $Re_\infty = 3.70 \times 10^6$ m^{-1}, $t = 3.79$ ms.

3.2. *Flow separation visualisation*

Steady SBLI flow-field images of all experimental results are displayed in figures 5 to 7. All images were truncated vertically to zoom in on the boundary layer. The x and y labels

https://doi.org/10.1017/jfm.2020.877 Published online by Cambridge University Press

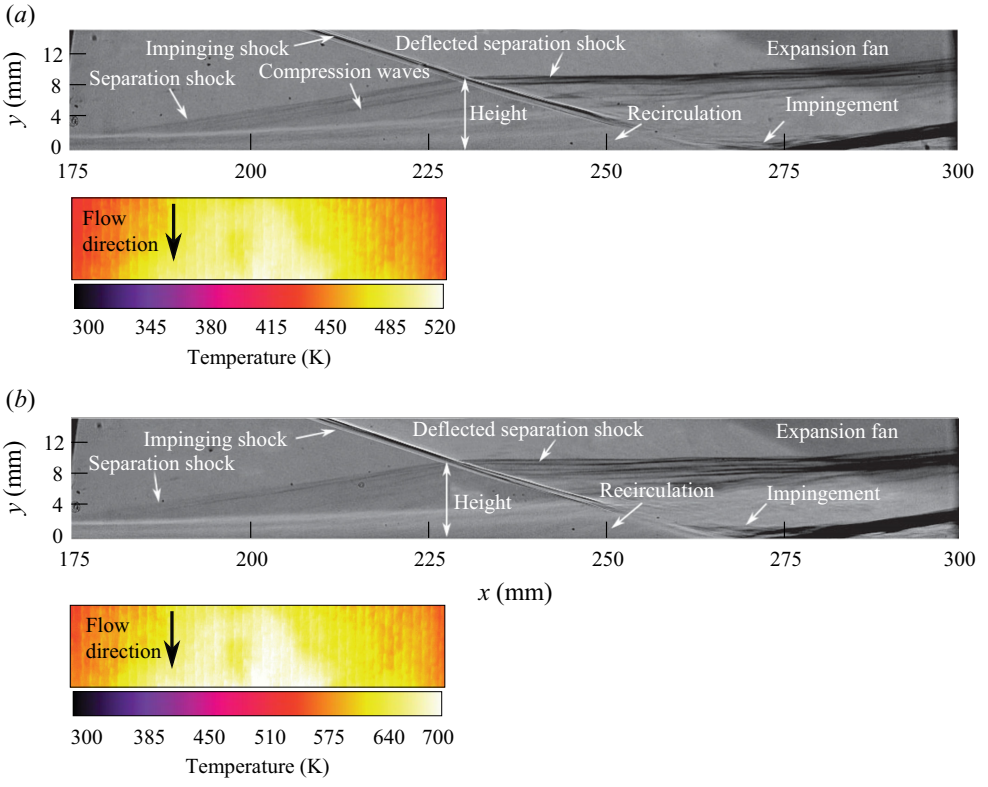


FIGURE 6. Heated model with impinging SBLI flow field: 12° shock generator. (*a*) Condition A, $T_w \approx 493$ K, $T_w/T_\infty \approx 1.98$, $T_w/T_r \approx 0.246$, $Re_\infty = 4.80 \times 10^6$ m^{-1}, $t = 3.58$ ms. (*b*) Condition A, $T_w \approx 664$ K, $T_w/T_\infty \approx 2.77$, $T_w/T_r \approx 0.343$, $Re_\infty = 5.30 \times 10^6$ m^{-1}, $t = 3.86$ ms.

are the streamwise distance from the flat plate leading edge and the height above the plate surface, respectively. Wall-to-recovery temperature ratio (T_w/T_r) and shot-specific Re_∞ are also included in the caption. The results presented herein are twofold: first with the unheated wall for all flow conditions, and next with the heated wall for the two different shock generator angle configurations.

Figure 5 shows the steady flow separation of unheated boundary layers for the 12° shock generator. Figure 5(*a*) depicts the separation shock, compression waves, flow recirculation and expansion fan in the flow field; these are the typical features of a large-scale laminar separation bubble that have been observed in previous studies (Sriram *et al.* 2016; Gai & Khraibut 2019). For the results shown in figure 5, the extent of separation depends highly on a combination of Re_∞ and T_w/T_∞. Conditions A and B have a similar T_w/T_∞; however, the lower $Re_\infty = 1.54 \times 10^6$ m^{-1} of Condition B induces a larger separation, as seen in figure 5(*b*). Also, the T_w/T_∞ values are obtained by changing T_∞, not by increasing T_w. This means the 'off-design' Condition D (figure 5*d*) has the lowest T_∞ and U_∞ and forms the thinnest boundary layer. Combined with a higher Re_∞, Condition D produces the smallest separation, as expected.

Figure 6 demonstrates the influence of the elevated T_w on flow separation for Condition A. Comparison of figures 5(*a*) and 6(*a*,*b*) reveals that L_{sep} grows first from 80 to 90 mm, and then to 107 mm, as the averaged T_w increases from 298 to 493 K, and then to

https://doi.org/10.1017/jfm.2020.877 Published online by Cambridge University Press

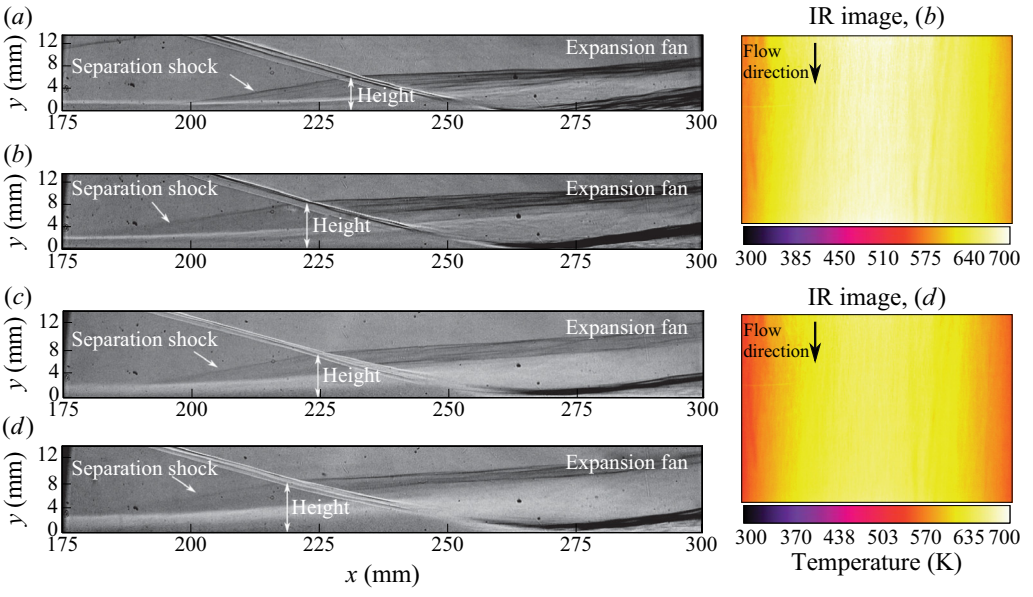


FIGURE 7. Heated model with impinging SBLI flow field: 10° shock generator. (*a*) Condition A, $T_w = 298$ K, $T_w/T_\infty = 1.25$, $T_w/T_r = 0.154$. (*b*) Condition A, $T_w \approx 675$ K, $T_w/T_\infty \approx 2.76$, $T_w/T_r \approx 0.342$. (*c*) Condition C, $T_w = 298$ K, $T_w/T_\infty = 1.89$, $T_w/T_r = 0.219$. (*d*) Condition C, $T_w \approx 639$ K, $T_w/T_\infty \approx 4.04$, $T_w/T_r \approx 0.466$.

664 K, respectively. With an upstream separation, the area enclosed by the separation shock and an impinging shock (the separation bubble) grows as well. In the recent flat plate testing of Chang *et al.* (2020), a thicker boundary layer formed when the wall was heated. A heated, thicker boundary layer has a lower density. Therefore, the adverse pressure from the impinging shock dissipates into a lower density, resulting in the separation shock forming at a more upstream location. Figure 7 shows that the wall heating increases L_{sep} with the 10° shock generator for Conditions A and C. The more upstream position of the shock generator allows a wider IR image field of view. Owing to the lower shock strength, the 10° shock generator configuration leads to smaller separation bubbles compared to the 12° results. Condition C has a lower Re_∞; therefore, for the unheated case (figure 7*c*), it produces a larger separation than Condition A (figure 7*a*). A high $T_w/T_\infty \approx 4.04$ could also be achieved when heated (figure 7*d*), allowing us to investigate a wider range of conditions.

For all conditions and configurations, the present experiment showcased that the separation bubbles for an impinging-shock flat plate in hypersonic flows grew with higher wall temperatures. The separation bubbles grew in both the streamwise direction and vertical height, which is consistent with the upstream shift in separation shock/pressure rise seen in other hot compression-ramp experiments (Elfstrom 1972; Bleilebens & Olivier 2006). The growth of separation observed in these flight-representative test flows suggests that increasing T_w will create larger separated regions when the shock impinges on any surface of the hypersonic vehicle in flight. These separations will block the scramjet internal flowpath and increase the local drag when the vehicle is operated for a longer duration, leading to a significant decrease in performance.

3.3. *Separation length scaling for hypersonic boundary layers*

There are few separation length correlations in the literature which incorporate the effect of T_w in SBLI. Katzer (1989) developed a correlation of the L_{sep} and pressure ratio across

https://doi.org/10.1017/jfm.2020.877 Published online by Cambridge University Press

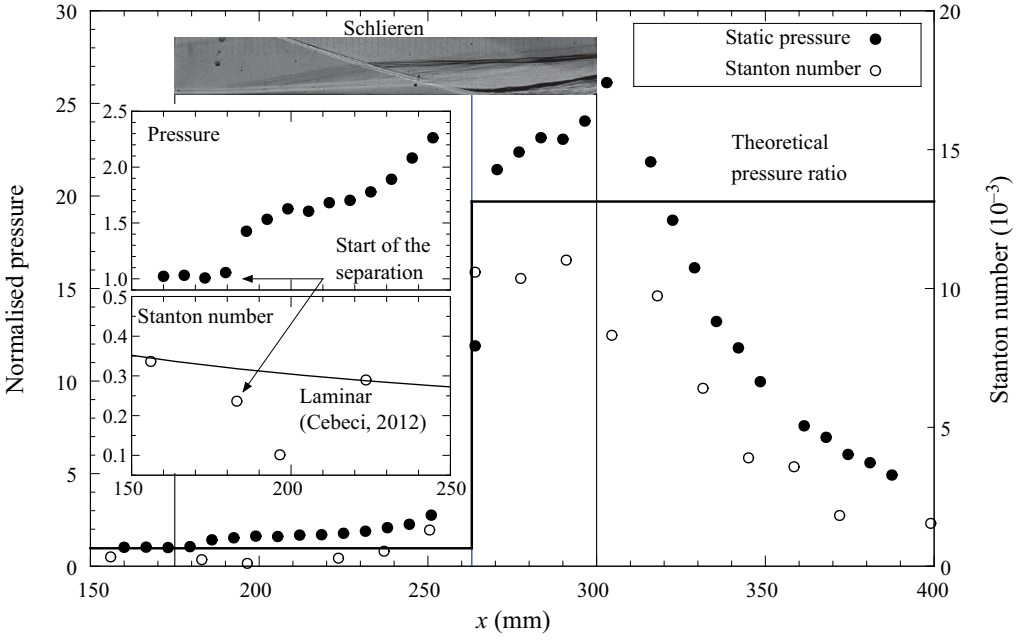


FIGURE 8. Mean surface properties: 12° shock generator, Condition A.

the shock from his numerical study of supersonic shock impingement. In the experimental investigation of the hypersonic heated compression ramp (Bleilebens & Olivier 2006), the scaled separation length (K) from the supersonic study (4.4) was modified as in (3.1) below to better account for the effect of elevated T_w:

$$\frac{L_{sep}}{\delta_i{}^*} = K\frac{\sqrt{\dfrac{Re_i}{C}}}{M_\infty^3}\left(\frac{p_r - p_{inc}}{p_\infty}\right), \quad K = 4.4 \; or \; 4.4 - 0.2\left(\frac{T_w}{T_\infty}\right). \tag{3.1}$$

Here, $\delta_i{}^*$ is the displacement thickness of the boundary layer. C is the Chapman–Rubesin constant, defined by the product of wall-to-free-stream viscosity ratio and free-stream-to-wall temperature ratio $(\mu_w/\mu_\infty)(T_\infty/T_w)$. The subscripts *inc*, i and r refer to the conditions at the start of the separation location, impingement (hinge line for compression ramp) location and reattachment, respectively. The ratio p_{inc}/p_∞ is determined by the approximation in Katzer (1989). Note that Bleilebens & Olivier (2006) used the values at *inc* for i, to better account for the free-interaction theory applying to their compression-ramp model. For the present configuration, the subscript i denotes the properties at the impingement; theoretical calculations determined the locations with shot-specific flow conditions. Then L_{sep} values measured from the shots, along with the isentropic flow relations to calculate p_s and theoretical boundary layer equations of Cebeci & Bradshaw (2012), are used to obtain K.

The mean surface properties of the instrumented plate are plotted in figure 8 to verify the use of theoretical calculations. The inset figure depicts the start of the separation at $x = 179.5$ mm, which is consistent with the linear fit from the schlieren image. Downstream of the onset of separation, the normalised pressure increases from 1.43 to 1.62 and then to 2.26, for $x = 186$ mm to $x = 199.5$ mm and $x = 244.5$ mm, respectively. The

https://doi.org/10.1017/jfm.2020.877 Published online by Cambridge University Press

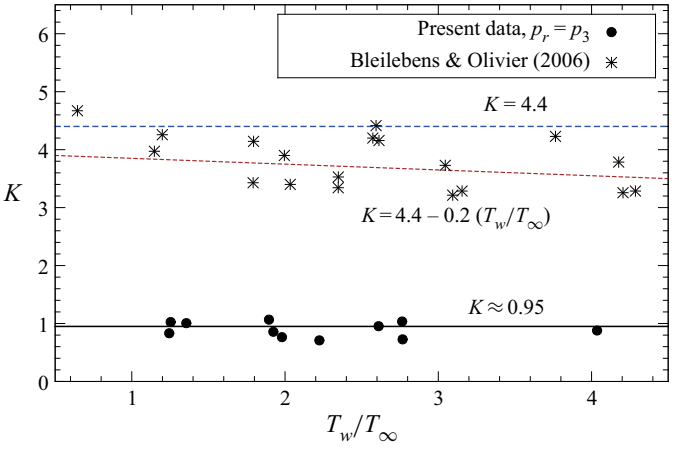


FIGURE 9. Separation length scaling of the present data with T_w/T_∞.

averaged value over this range is 1.76. This closely matches the supersonic approximation of Katzer (1989) for the same flow condition ($p_{inc}/p_w = 1.79$). Even with the flow separation, the static pressure traces were fairly steady with time in these locations. The normalised pressure just behind the reflected shock (reattachment pressure) at $x =$ 270.5 mm is 21.4, which is 8.8 % higher than the theoretical pressure ratio across the shock (p_3/p_w). This disagreement could be attributed to experimental uncertainty and to shock-induced transition producing slightly higher pressures in the reattachment (Bleilebens & Olivier 2006; Currao *et al.* 2020). Hence, the theoretical ratio could be employed for the present study. The Stanton number distribution shows that the upstream boundary layer is laminar. At $x = 183$ mm and $x = 196.5$ mm the Stanton number values decrease due to the thickening of the boundary layer. The shock impingement incites the turbulent transition. Maximum heat transfer is experienced until the expansion fan from the trailing edge of the shock generator reaches the plate at $x \approx 318$ mm.

Figure 9 compares K versus T_w/T_∞ of the present work against prior separation length correlations. The present data show good agreement with a constant $K \approx 0.95$. The effect of T_w is mainly determined by C in (3.1). For the present study, the C values range from 0.75 to 0.95. The square root of the C values is from 0.87 to 0.97, which is close to 1. Therefore, K that is proportional to $\sqrt{C}$ shows a weak T_w influence. The flow regimes are also different, with the supersonic scaling of Katzer (1989) based on M_∞ from 1.4 to 3.4, p_r/p_∞ from 1.2 to 1.8 and Re_i from 1×10^5 to 6×10^5. Hypersonic scaling (Bleilebens & Olivier 2006) from the compression-corner study was based on M_∞ from 7.1 to 8.1, p_r/p_∞ from 7.03 to 11.5 (calculated from their experimentally measured coefficient of pressure $c_p \approx 0.2$ to $c_p \approx 0.25$) and Re_i from approximately 3.3×10^5 to 3.8×10^5. The p_r of the hypersonic compression ramp is effectively p_2, which is the pressure behind the ramp shock, whereas the p_r of the shock impingement correlation is effectively p_3, because the reattachment occurs after an additional compression from the reflected shock. Hence, a higher p_3/p_∞ value of 14 to 22.1 and Re_i of 4.1×10^5 to 13×10^5 for the present data, divided by $L_{sep}/\delta_i{}^*$, lead to a smaller K. The findings demonstrate that the flow separation length in hypersonic impinging SBLI with heated walls is influenced by the higher shock strength (measured by the pressure ratio), and cannot be easily deduced from previous supersonic impinging SBLI or hypersonic compression-ramp correlations.

https://doi.org/10.1017/jfm.2020.877 Published online by Cambridge University Press

4. Conclusions

This work showcased the effect of elevated wall temperatures in hypersonic impinging SBLI in Mach 7 flight-representative flows of the T4 shock tunnel. The test model was reliably heated and produced a large-scale, steady separation bubble during the facility test-time. By inspecting flow structures captured in schlieren images and using the transition criteria of T4, the unheated SBLI data in this work were all obtained with laminar flow. The 12° shock generator SBLI flow field for various flow conditions indicated a significant influence of Reynolds number on flow separation. For a fixed free-stream temperature and Reynolds number, a clear increase in separation length with increasing wall temperature was observed. Experiments with a 10° shock generator also showed a decrease in the extent of separation compared to the 12° cases, yet the higher wall temperature enlarged the separation. Existing correlations for laminar separation length as a function of wall temperature were also applied to the present data. A high discrepancy was observed between the current work and correlations from both the separation scaling of supersonic impinging shocks and its modification for the hypersonic compression ramp, mainly because of the higher shock strength in the present experiments, highlighting the need for additional data sets spanning more conditions in order to improve existing correlations. The increase of flow separation with elevated wall temperature is an important result for the future design and testing of scramjet flowpaths and hypersonic vehicles where this phenomenon must be considered.

Acknowledgements

The work was sponsored by the UQ–National University of Singapore Research Collaboration and the Air Force Office of Scientific Research under award number FA9550-18-1-0265, with Dr I. Leyva as the project manager. The computational resources were provided by the NCI Facility under the National Computational Merit Allocation Scheme, supported by the Australian Government. The authors acknowledge K. Hitchcock for technical support and T4 operators R. Whitside, A. Ward, I. Convery-Brien, R. Ananthapadmanaban and K. Hopkins for operating the T4 Stalker Tube facility. Special thanks to K. Hopkins for operating the power supply and helping with the IR calibration. E.W.K.C. acknowledges support through the University of Queensland Research Training Scholarship.

Declaration of interests

The authors report no conflict of interest.

References

Billig, F. S. 1993 Research on supersonic combustion. *J. Propul. Power* **9** (4), 499–514.

Bleilebens, M. & Olivier, H. 2006 On the influence of elevated surface temperatures on hypersonic shock wave/boundary layer interaction at a heated ramp model. *Shock Waves* **15** (5), 301–312.

Boyce, R. R, Takahashi, M. & Stalker, R. J. 2005*a* Mass spectrometric measurements of driver gas arrival in the T4 free-piston shock-tunnel. *Shock Waves* **14** (5–6), 371–378.

Boyce, R. R, Takahashi, M. & Stalker, R. J. 2005*b* Mass spectrometric measurements of the freestream composition in the T4 free-piston shock-tunnel. *Shock Waves* **14** (5–6), 359–370.

Cebeci, T. & Bradshaw, P. 2012 *Physical and Computational Aspects of Convective Heat Transfer*. Springer.

https://doi.org/10.1017/jfm.2020.877 Published online by Cambridge University Press

CHAN, W. Y. K., JACOBS, P. A., SMART, M. K., GRIEVE, S., CRADDOCK, C. S. & DOHERTY, L. J. 2018 Aerodynamic design of nozzles with uniform outflow for hypervelocity ground-test facilities. *J. Propul. Power* **34** (6), 1467–1478.

CHANG, E. W. K., CHAN, W. Y. K., HOPKINS, K. J., MCINTYRE, T. J. & VEERARAGAVAN, A. 2020 Electrically-heated flat plate testing in a free-piston driven shock tunnel. *Aerosp. Sci. Technol.* **102**, 1–11.

CHANG, E. W. K., CHAN, W. Y. K., MCINTYRE, T. J. & VEERARAGAVAN, A. 2019 Hypersonic shock impingement on a heated surface in T4 free-piston driven shock tunnel. In *32nd International Symposium on Shock Waves*, pp. 89–95. Research Publishing Services.

CURRAO, G. M. D., CHOUDHURY, R., GAI, S. L., NEELY, A. J. & BUTTSWORTH, D. R. 2020 Hypersonic transitional shock-wave-boundary-layer interaction on a flat plate. *AIAA J.* **58** (2), 814–829.

DOLLING, D. S. 2001 Fifty years of shock-wave/boundary-layer interaction research: what next? *AIAA J.* **39** (8), 1517–1531.

ELFSTROM, G. M. 1972 Turbulent hypersonic flow at a wedge-compression corner. *J. Fluid Mech.* **53**, 113–127.

GAI, S. L. & KHRAIBUT, A. 2019 Hypersonic compression corner flow with large separated regions. *J. Fluid Mech.* **877**, 471–494.

HOLDEN, M. S. 1971 Establishment time of laminar separated flows. *AIAA J.* **9** (11), 2296–2298.

JACOBS, P. A., GOLLAN, R. J., POTTER, D. F., ZANDER, F., GILDFIND, D. E., BLYTON, P., CHAN, W. Y. K. & DOHERTY, L. 2014 Estimation of high-enthalpy flow conditions for simple shock and expansion processes using the ESTCj program and library. *Tech. Rep.* 2011/02. Centre for Hypersonics, The University of Queensland.

JAUNET, V., DEBIEVE, J. & DUPONT, P. 2014 Length scales and time scales of a heated shock-wave/boundary-layer interaction. *AIAA J.* **52** (11), 2524–1741.

KATZER, E. 1989 On the lengthscales of laminar shock/boundary-layer interaction. *J. Fluid Mech.* **206**, 477–496.

KNISELY, A. M. & AUSTIN, J. M. 2016 Geometry and test-time effects on hypervelocity shock-boundary layer interaction. *AIAA Paper* 2016-1979.

MALLINSON, S. G., GAI, S. L. & MUDFORD, N. R. 1997 Establishment of steady separated flow over a compression–corner in a free–piston shock tunnel. *Shock Waves* **7** (4), 249–253.

MEE, D. J. 1993 Uncertainty analysis of conditions in the test section of the T4 shock tunnel. *Tech. Rep.* 1993/04. Centre for Hypersonics, University of Queensland.

SANDHAM, N. D., SCHÜLEIN, E., WAGNER, A., WILLEMS, S. & STEELANT, J. 2014 Transitional shock-wave/boundary-layer interactions in hypersonic flow. *J. Fluid Mech.* **752**, 349–382.

SCHÜLEIN, E. 2006 Skin friction and heat flux measurements in shock/boundary layer interaction flows. *AIAA J.* **44** (8), 1732–1741.

SRIRAM, R. & JAGADEESH, G. 2015 Correlation for length of impinging shock-induced large separation bubble at hypersonic speed. *AIAA J.* **53** (9), 2771–2776.

SRIRAM, R., SRINATH, L., DEVARAJ, M. K. K. & JAGADEESH, G. 2016 On the length scales of hypersonic shock-induced large separation bubbles near leading edges. *J. Fluid Mech.* **806**, 304–355.

STALKER, R. J., PAULL, A., MEE, D. J., MORGAN, R. G. & JACOBS, P. A. 2005 Scramjets and shock tunnels – the Queensland experience. *Prog. Aerosp. Sci.* **41** (6), 471–513.

SWANTEK, A. B. & AUSTIN, J. M. 2015 Flowfield establishment in hypervelocity shock-wave/boundary-layer interactions. *AIAA J.* **53** (2), 311–320.

VOLPIANI, P. S., BERNARDINI, M. & LARSSON, J. 2020 Effects of a nonadiabatic wall on hypersonic shock/boundary-layer interactions. *Phys. Rev. Fluids* **5**, 1–20.

WAGNER, A., SCHRAMM, J. M., HANNEMANN, K., WHITSIDE, R. W. & HICKEY, J. 2018 Hypersonic shock wave boundary layer interaction studies on a flat plate at elevated surface temperature. In *Shock Wave Interactions* (ed. K. Kontis), pp. 231–243.

https://doi.org/10.1017/jfm.2020.877 Published online by Cambridge University Press